Photoacoustic Molecular Imaging for the Identification of Lymph Node Metastasis in Head and Neck Cancer Using an Anti-EGFR Antibody–Dye Conjugate

Naoki Nishio[1,2], Nynke S. van den Berg[1], Brock A. Martin[3], Stan van Keulen[1], Shayan Fakurnejad[1], Eben L. Rosenthal[1], and Katheryne E. Wilson[4]

[1]Department of Otolaryngology–Head and Neck Surgery, Stanford University School of Medicine, Stanford, California; [2]Department of Otorhinolaryngology, Nagoya University Graduate School of Medicine, Nagoya, Aichi, Japan; [3]Department of Pathology, Stanford University School of Medicine, Stanford, California; and [4]Department of Radiology, Stanford University School of Medicine, Stanford, California

The presence of lymph node (LN) metastases is an essential prognostic indicator in patients with head and neck squamous cell carcinoma (HNSCC). This study assessed photoacoustic molecular imaging (PAMI) of the antiepidermal growth factor receptor antibody (panitumumab) conjugated to a near-infrared fluorescent dye, IRDye800CW (panitumumab-IRDye800CW; pan800), for the identification of occult metastatic LNs in patients with HNSCC ($n = 7$). **Methods:** After in vitro photoacoustic imaging characterization of pan800, PAMI was performed on excised neck specimens from patients infused with pan800 before surgery. Freshly obtained neck specimens were imaged with 3-dimensional, multiwavelength spectroscopic PAMI (wavelengths of 680, 686, 740, 800, 860, 924, and 958 nm). Harvested LNs were then imaged with a closed-field near-infrared fluorescence imager and histologically examined by the pathologist to determine their metastatic status. **Results:** In total, 53 LNs with a maximum diameter of 10 mm were analyzed with photoacoustic and fluorescence imaging, of which 4 were determined to be metastatic on the final histopathologic report. Photoacoustic signals in the LNs corresponding to accumulated pan800 were spectrally unmixed using a linear least-square-error classification algorithm. The average thresholded photoacoustic signal intensity corresponding to pan800 was 5-fold higher for metastatic LNs than for benign LNs (2.50 ± 1.09 arbitrary units [a.u.] vs. 0.53 ± 0.32 a.u., $P < 0.001$). Fluorescence imaging showed that metastatic LNs had a 2-fold increase in fluorescence signal compared with benign LNs ex vivo ($P < 0.01$, 0.068 ± 0.027 a.u. vs. 0.035 ± 0.018 a.u.). Moreover, the ratio of the average of the highest 10% of the photoacoustic signal intensity over the total average, representative of the degree of heterogeneity in the pan800 signal in LNs, showed a significant difference between metastatic LNs and benign LNs (11.6 ± 13.4 vs. 1.8 ± 0.7, $P < 0.01$) and an area under the receiver-operating-characteristic curve of 0.96 (95% CI, 0.91–1.00). **Conclusion:** The data indicate that PAMI of IRDye800-labeled tumor-specific antibody may have the potential to identify occult LN metastasis perioperatively in HNSCC patients.

Key Words: photoacoustic imaging; head and neck cancer; lymph node; antibody–dye; near-infrared

J Nucl Med 2021; 62:648–655
DOI: 10.2967/jnumed.120.245241

The presence of lymph node (LN) metastases is an essential prognostic indicator in patients with head and neck squamous cell carcinoma (HNSCC) (*1*). Despite the clinical use of various imaging modalities for preoperative nodal staging, such as CT and MRI, these imaging techniques lack the specificity to detect occult metastases in nodes with axial diameters smaller than 10 mm (*2–5*). Moreover, to warrant accurate nodal staging, postoperative pathologic processing may require as many as 18 LNs to be harvested from resected neck specimens after dissection for subsequent evaluation by pathologists (*6*). Taken together, the current treatment workflow for LN management in HNSCC requires an elective neck dissection of curative intent (*7,8*) and a careful evaluation of all harvested LNs with a final pathologic or histopathologic report (*9*), resulting in lower quality-of-life scores for patients because of potentially poor cosmetic outcomes, dysfunction of the spinal accessory nerve, and prolonged pain, as well as increased health-care costs due to increased labor and use of equipment and supplies (*10*).

Recently, it was demonstrated that near-infrared (NIR) fluorescence imaging of an antiepidermal growth factor receptor (EGFR) antibody conjugated to IRDye800CW intravenously injected several days before surgery was able to distinguish metastatic from benign LNs with a high sensitivity and specificity in an ex vivo, pathologic, setting (*11*). However, challenges remain in translating these findings into an intraoperative setting. Cervical LNs are located at a depth of up to several centimeters in the human neck, and therefore, the limited penetration depth of NIR light into human tissue (limited to <7 mm) makes it challenging to noninvasively assess the neck even in an intraoperative setting (*12*).

Photoacoustic molecular imaging (PAMI) is a hybrid imaging technology that combines the imaging depth of ultrasound (≤5 cm) with the contrast and molecular imaging capabilities of optical imaging. On the basis of the photoacoustic effect (*13*), nanosecond pulsed laser irradiation is used to induce transient, localized thermal

Received Mar. 17, 2020; revision accepted Aug. 27, 2020.
For correspondence or reprints contact: Katheryne E. Wilson, Stanford University School of Medicine, 3155 Porter Dr., Palo Alto, CA 94304.
E-mail: wilsonk2@stanford.edu
Published online Oct. 2, 2020.

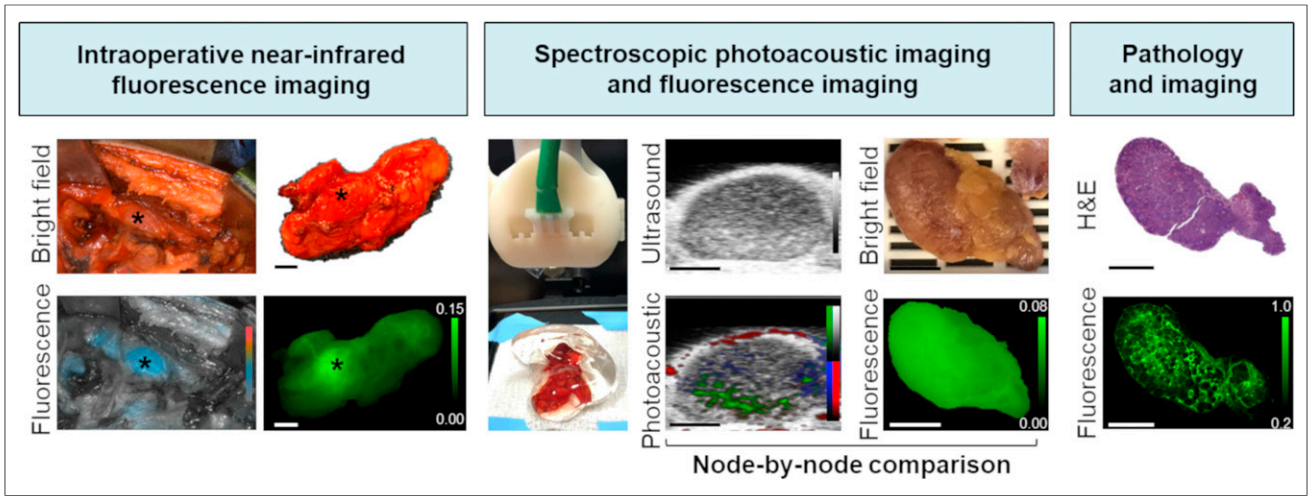

FIGURE 1. Workflow of photoacoustic and fluorescence imaging of pan800 in HNSCC and LNs, including intraoperative, postoperative, and histologic imaging. All scale bars are 5 mm. H&E = hematoxylin and eosin.

expansion through optical absorption by native or exogenous chromophores, resulting in the production of ultrasonic waves that can be detected using standard ultrasound transducers (*14–16*). Furthermore, as the optical absorption is wavelength-dependent, multiwavelength, spectroscopic PAMI can be implemented to examine signal corresponding to a single chromophore of interest, such as a NIR dye, while suppressing background blood-pool signal. Combined photoacoustic and fluorescence molecular imaging of specific cell-surface targets using antibodies conjugated to NIR dyes is thus a new and promising approach. Previous reports indicated that combined photoacoustic and fluorescent molecular imaging using an anti-B7-H3 antibody–NIR dye conjugate could differentiate clinically actionable breast carcinoma and ductal carcinoma in situ from normal mammary tissues in a transgenic murine model of breast cancer (*17–19*). Hence, it is hypothesized that the highly specific imaging ability of spectroscopic PAMI combined with a preoperatively administered molecularly tumor-specific contrast agent can be leveraged to improve noninvasive identification of occult LN metastasis in HNSCC patients. Moreover, this photoacoustic approach may be used to guide surgeons' selection of affected LNs immediately after LN dissection. The current study explored the potential of PAMI and NIR fluorescence imaging of the IRDye800CW-labeled anti-EGFR antibody (panitumumab-IRDye800CW; pan800) for the ex vivo identification of metastatic LNs in nodal specimens obtained from HNSCC patients that were infused with pan800 1–5 d before surgery.

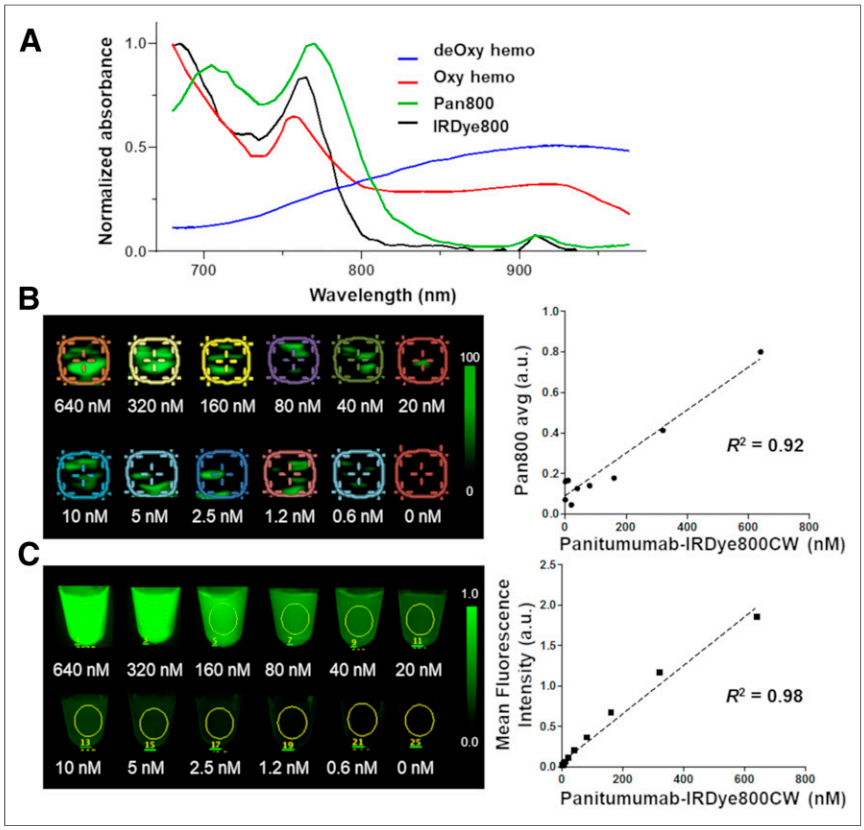

FIGURE 2. Determining optical absorption spectra (A) and photoacoustic (B) and fluorescence (C) imaging sensitivity for pan800. deOxy hemo = deoxygenated hemoglobin; Oxy hemo = oxygenated hemoglobin.

MATERIALS AND METHODS

Clinical Study Overview

As part of an ongoing phase I study (NCT02415881), combined PAMI and NIR fluorescence imaging of pan800 was evaluated for determining LN status in HNSCC patients scheduled to undergo a curative primary-tumor resection with a subsequent elective neck dissection. An overview of the clinical workflow is depicted in Figure 1. A node-by-node comparison between PAMI and NIR fluorescence imaging and histopathologic

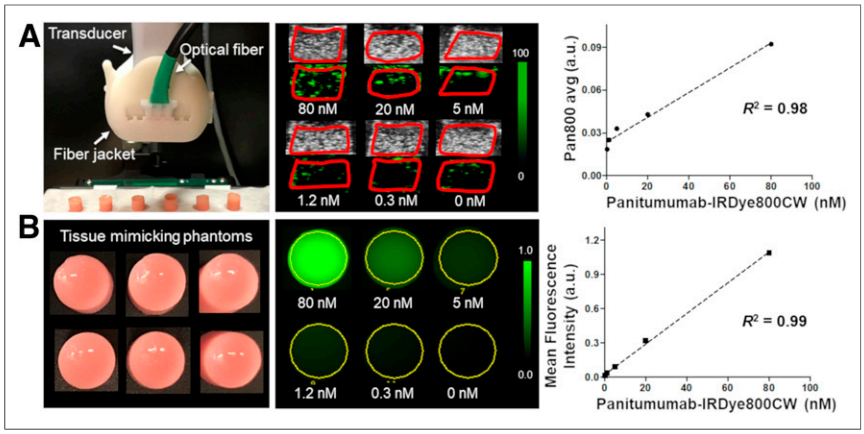

FIGURE 3. Photoacoustic (A) and fluorescence (B) imaging of decreasing concentrations of pan800 in tissue-mimicking phantom. avg = average.

LN status was performed. LNs 2–10 mm thick were included in this study because of the clinical significance of finding occult metastases in small LNs with a diameter of less than 10 mm.

The study protocol was approved by the Stanford University Administrative Panel on Human Subjects Research. The study was performed in accordance with the Helsinki Declaration of 1975 and its amendments, the Food and Drug Administration's International Conference on Harmonization Good Clinical Practice guidelines, and the laws and regulations of the United States. Written informed consent was obtained from all patients. The anti-EGFR antibody–NIR dye conjugate (pan800) was conjugated under current good-manufacturing-practice conditions as previously described (*20*).

In Vitro PAMI Characterization of Panitumumab-IRDye800CW

Before PAMI was performed on human neck specimens, the photoacoustic absorption spectrum of pan800 and the sensitivity of the Vevo LAZR-X imaging system (Fujifilm VisualSonics) to pan800 was tested in a polymetric blood vessel–mimicking phantom (Fig. 2). Polyethylene plastic tubes (50 μL per tube; Fujifilm VisualSonics) were filled with pan800 solutions (concentrations from 0 to 640 nM; diluted 1:1 in deionized water) in the phantom imaging chamber filled with deionized water. Photoacoustic and corresponding ultrasound images were acquired with the 20-MHz linear array transducer at wavelengths from 680 to 970 nm in 10-nm increments. Regions of interest were placed over the tubing in coregistered ultrasound images, and photoacoustic signal intensity was measured and plotted against concentration. To acquire the reference spectrum of pan800, the photoacoustic signal intensity over the wavelength within the highest-concentration solution was plotted to provide the absorption spectra of pan800 as detected by the imaging system.

Next, to more closely recapitulate imaging and sensitivity limitations in an in vivo situation, an agarose-based, tissue-mimicking phantom (6-mm diameter, acoustic attenuation similar to that of LNs [~1.5 $dB \cdot MHz^{-1} \cdot cm^{-1}$] (*21*,*22*)) comprising 1% agarose (LifeTechnologies), 1% whole bovine blood (Sigma-Aldrich), 1% intralipid emulsion (Sigma-Aldrich), 0.1% silica, and varying concentrations of pan800 (0, 0.3, 1.2, 5, 20, and 80 nM) was synthesized as previously described (*23*). The Vevo LAZR-X system paired with the 20-MHz transducer was used to take cross-sectional images at maximal diameter at wavelengths from 680 to 970 nm. Phantoms were coupled to the transducer with clear, colorless, bubble-free ultrasound gel (LithoClear), and the surface of the phantoms was maintained at 9 mm from the surface of the transducer to confer optimal illumination. Spectroscopic PAMI thresholds (range, 0–100 arbitrary units [a.u.]) for the phantom experiment were as follows: for measuring photoacoustic signal intensity from pan800, brightness was set to 60, opacity to 99, contrast to 90, and threshold to 80. For deoxygenated hemoglobin measurements, brightness was set to 58, opacity to 70, contrast to 90, and threshold to 80. For oxygenated hemoglobin measurements, the respective numbers were 53, 99, 80, and 95.

To validate the presence of pan800, phantoms were placed on a black imaging tray and fluorescence imaging of pan800 was performed in a closed-field fluorescence imaging device (Pearl Trilogy; LI-COR Biosciences Inc.).

Intraoperative NIR Fluorescence Imaging of LNs

Intraoperative fluorescence imaging was performed before, during, and after neck dissection using the handheld imaging device (SPY-PHI; Novadaq) and optical imaging platform (IR9000; Novadaq) optimized for the detection of IRDye800CW as described previously (*24*).

Spectroscopic Photoacoustic Imaging of LNs

PAMI of whole neck specimens was performed ex vivo immediately after surgical resection (<25 min). PAMI data were acquired on a Vevo LAZR-X imaging system with a 20-MHz (13–24 MHz) linear array transducer (MX 250; axial resolution, 75 μm). The narrow optical fiber (14 mm) was used to maximize light penetration and imaging depth. Surgically collected nodal specimens were imaged at 7 wavelengths (680, 686, 740, 800, 860, 924, and 958 nm, optimized to minimize scan time while allowing for accurate spectral classification) with 10-ns pulses, a 20-Hz pulse repetition frequency, a persistence of 2, and a measured fluence of 150 mJ/cm^2. For 3-dimensional image acquisition, the transducer was automatically scanned over the resected neck specimen by a stepping motor with a step size of 0.5 mm. Spectroscopic imaging thresholds (range, 0–100) were maintained at the following values. For photoacoustic signal intensity from pan800, brightness was set to 50 (primary tumor brightness was set to 60), opacity to 99, contrast to 90, and threshold to 80. For deoxygenated hemoglobin measurements, brightness was set to 50, opacity to 70, contrast to 90, and threshold to 80. For oxygenated hemoglobin measurements, the respective numbers were 50, 99, 80, and 95.

After PAMI, the molecular imaging signal corresponding directly to pan800 accumulation was measured with Vevo LAB software (version 2.2.0; Fujifilm VisualSonics). Regions of interest were drawn on 3 consecutive imaging planes over the entire area of maximal axial planes in each LN (or primary tumor specimen) on the corresponding

TABLE 1
Patient Characteristics

Patient no.	Age (y)	Sex	Tumor location	cTN stage
1	70	Female	Buccal mucosa	T3N0
2	68	Female	Lateral tongue	T3N2b
3	71	Female	Lateral tongue	T1N0
4	47	Female	Retromolar trigone	T4N2b
5	56	Male	Buccal mucosa	T2N0
6	60	Male	Ear	T2N0
7	70	Male	Lateral tongue	T3N0

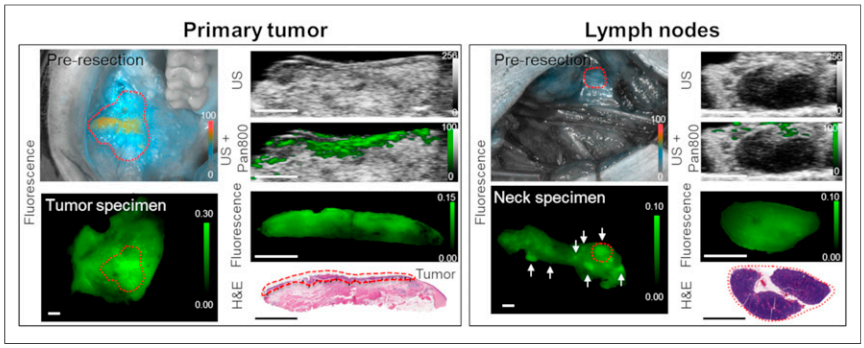

FIGURE 4. Fluorescence, spectroscopic photoacoustic pan800 signal, and histology images from representative patient with primary tumor and benign LNs. Tumor is outlined in red dashed line. White arrows represent locations of several LNs within neck specimen; red dashed circle highlights the LN shown by histology at the bottom right. All scale bars are 5 mm. H&E = hematoxylin and eosin; US = ultrasound.

B-mode ultrasound images by a researcher familiar with head and neck ultrasound. Next, images underwent spectral unmixing of oxygenated hemoglobin, deoxygenated hemoglobin (absorbance-based reference spectra), and pan800 (using the previously determined reference spectra). The software automatically calculated the average signal intensity of all the pixels corresponding to pan800 (pan800 avg), the average of the top 10% of the photoacoustic signal intensity corresponding to pan800 (pan800 avg thresh), the average total hemoglobin signal, and the average total oxygen saturation. Molecular imaging signal values from 3 cross sections for each LN were averaged for use in further statistical and receiver-operating-curve (ROC) analysis.

Closed-Field NIR Fluorescence Imaging of Harvested LNs

In addition to PAMI of the resected LN tissues, NIR fluorescence imaging of harvested LNs was performed before the process of paraffin embedding using a closed-field NIR optical imaging system (Pearl Trilogy), in which the imaging environment could control for ambient light and the fix the camera–tissue distance with an 800-nm channel (*12*). After imaging, mean fluorescence intensities, defined as total counts per region-of-interest pixel area, was calculated for each LN using the system's integrated software (Image Studio; LI-COR Biosciences Inc.) to perform quantitative analysis of closed-field fluorescence imaging data (*11*).

Pathology Preparation and Imaging

Next, the metastatic status of the resected LNs was determined. After processing and paraffin embedding, 4-μm-thick sections were sliced and stained with hematoxylin and eosin. The hematoxylin-and-eosin slides were reviewed by a board-certificated pathologist, who outlined the tumor boundaries and identified cancerous regions. The Odyssey imaging platform (LI-COR Biosciences Inc.) was used to assess fluorescence in slide-mounted sections obtained from formalin-fixed paraffin-embedded blocks (*11*).

Statistical Analysis

Descriptive statistics and figures were obtained using Prism (version 6.0c; GraphPad Software). Data are presented as box plots with whiskers depicting minimum to maximum values. All data points are displayed. Differences in ultrasound, PAMI, and fluorescence imaging between metastatic and benign LNs were analyzed with the Mann–Whitney *U* test. The correlation between the ultrasound area and the pathologic area was determined using nonparametric Spearman correlation. All data are presented as mean or as mean ± SD, and a 2-sided *P* value of 0.05 or less was considered statistically significant.

RESULTS

Validation of PAMI and NIR Fluorescence Imaging Using Panitumumab-IRDye800CW

Using a polymetric blood vessel–mimicking phantom, the optical absorption spectra of pan800 was determined by plotting absorption over wavelength. The pan800 reference spectrum as determined through PAMI was shown to have dual peaks at 710 and 770 nm, compared with oxygenated and deoxygenated hemoglobins, which have peaks at 750 and 900 nm, respectively, as graphed in Figure 2A. A strong correlation was found between the dose of pan800 and the detected photoacoustic molecular signal (pan800 avg, R^2 = 0.92; Fig. 2B). For a reference, fluorescence imaging of the pan800 phantom also demonstrated the strong correlation between mean fluorescence intensity and pan800 concentration (R^2 = 0.98; Fig. 2C). PAMI was able to detect down to 1.2 nM pan800.

Next, a decreasing-concentration study (80–0 nM) using a tissue-mimicking phantom was implemented to determine the sensitivity limit of the Vevo LAZR-X and the Pearl Trilogy system for pan800. The dose of pan800 correlated strongly with the detected photoacoustic signal (pan800 avg, R^2 = 0.98; Fig. 3A) and with the mean fluorescence intensity (R^2 = 0.99; Fig. 3B).

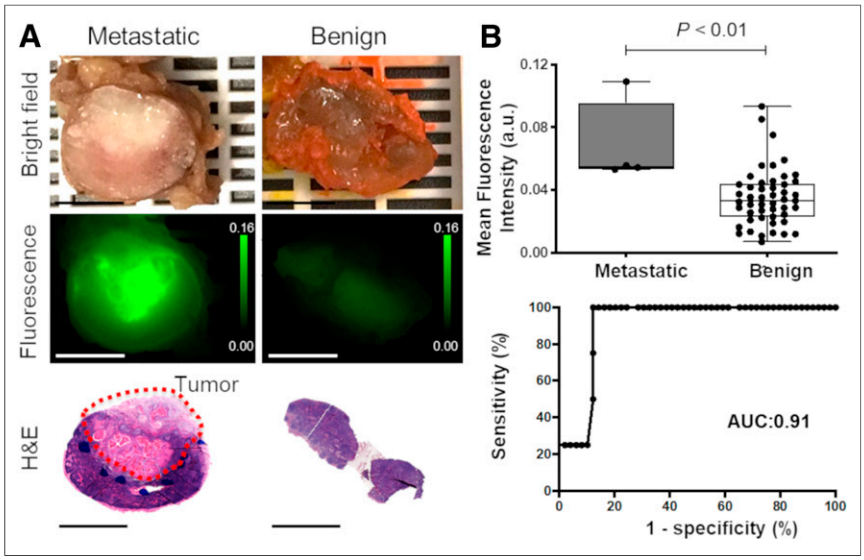

FIGURE 5. Discrimination of metastatic LNs from benign LNs from head and neck cancer patients using fluorescence imaging. (A) Bright-field and fluorescence images of metastatic and benign LNs corresponding to hematoxylin-and-eosin slides. (B) Quantitative analysis of mean fluorescence intensity for differentiating benign from metastatic LNs. All scale bars are 5 mm. H&E = hematoxylin and eosin.

PAMI was able to detect pan800 concentrations of as low as 1.2 nM.

Patient and LN Characteristics

Between June 2018 and February 2019, 7 patients were enrolled in this study. Their characteristics are provided in Table 1. All patients received a fixed 50-mg dose of pan800 at a mean of 2 d before surgery (range, 1–5 d). Figure 4 shows the photoacoustic and fluorescence images of a representative patient with oral squamous cell carcinoma who underwent primary tumor resection and neck dissection.

In total, from the 14 collected neck specimens from 7 consecutive patients, 53 LNs 2–10 mm thick were imaged using photoacoustic and closed-field NIR fluorescence imaging and analyzed. On the final histopathologic report, 4 of the 53 LNs were found to harbor metastatic disease.

The ultrasound-determined thickness of metastatic LNs was 6.8 ± 2.5 mm, which was statistically significantly greater than that of benign LNs (3.7 ± 1.6 mm, $P < 0.01$; Supplemental Fig. 1A [supplemental materials are available at http://jnm.snmjournals.org]). Additionally, a strong correlation was found between the ultrasound-determined area and the area as measured on final histologic examination ($R^2 = 0.83$, $P < 0.01$; Supplemental Fig. 1B), demonstrating a matched comparison of collected LNs confirmed by histology.

Discrimination of Metastatic from Benign LNs on Closed-Field NIR Fluorescence Imaging

The ex vivo fluorescence signal corresponding to pan800 was 2-fold higher for metastatic LNs than for benign LNs ($P < 0.01$, 0.068 ± 0.027 a.u. vs. 0.035 ± 0.018 a.u.; Fig. 5). Statistical analysis for mean fluorescence intensity from NIR fluorescence imaging yielded a sensitivity of 100% and specificity of 87.8%. ROC evaluation showed an area under the curve (AUC) of 0.91 (95% CI, 0.82–0.99).

Photoacoustic-Signal Differentiation of Metastatic from Benign LNs

Spectroscopic PAMI was used to comparatively quantify the signal from pan800 accumulated in benign and metastatic LNs. Figure 6A shows representative photoacoustic images of benign and metastatic LNs with spectroscopically resolved pan800 and oxy- and deoxyhemoglobin signal. The pan800 avg did not significantly differ between metastatic and benign LNs, at 0.51 ± 0.48 a.u. vs. 0.36 ± 0 0.21 a.u., respectively ($P > 0.05$; Fig. 6B). ROC evaluation showed that the AUC for the pan800 avg was 0.61 (95% CI, 0.23–0.99). However, metastatic LNs had a 5-fold increase in pan800 avg thresh compared with benign LNs ($P < 0.01$, 2.50 ± 1.09 a.u. vs. 0.53 ± 0.32 a.u.; Fig. 6C). ROC evaluation showed that the AUC for pan800 avg thresh was 1.00 (95% CI,

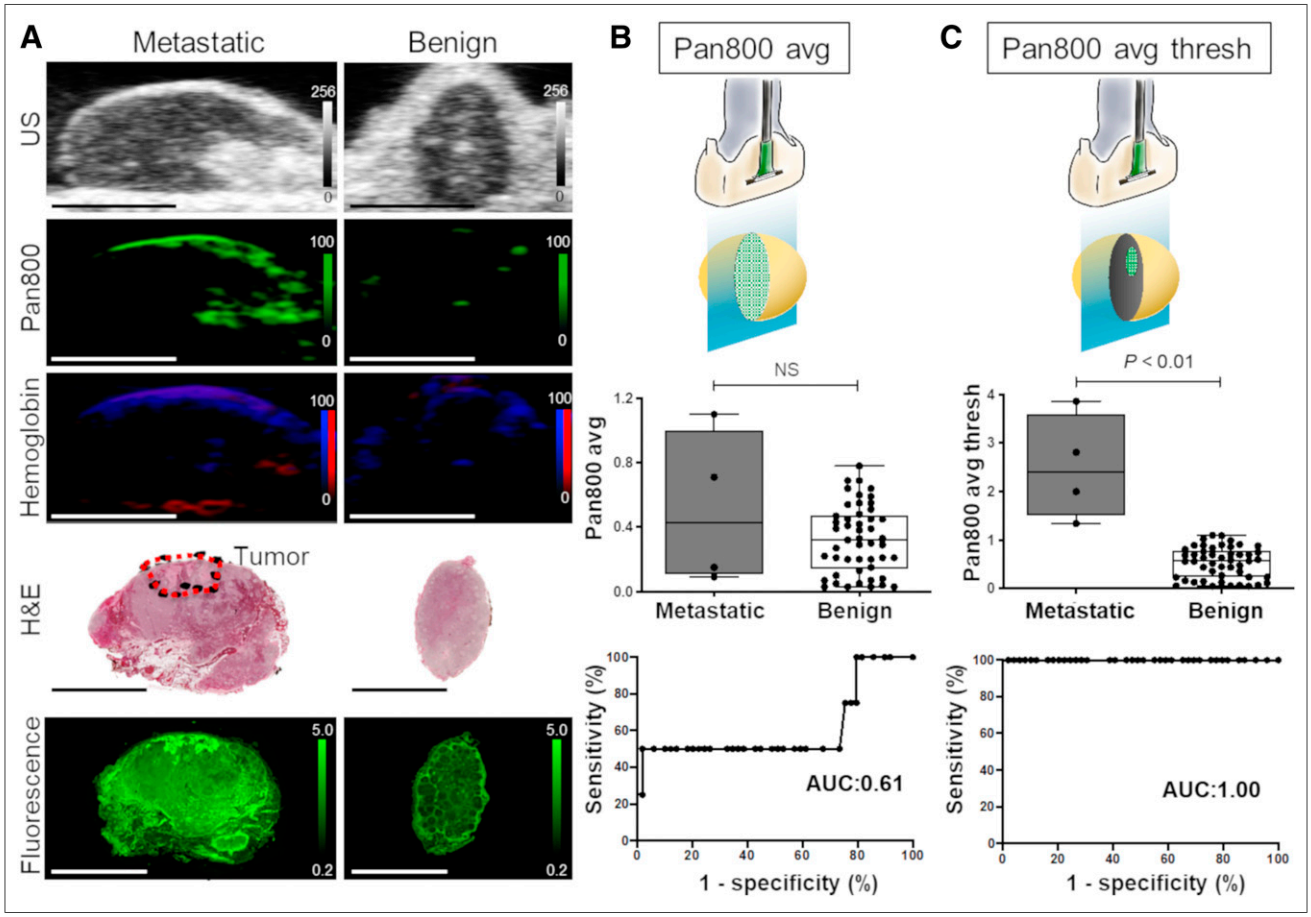

FIGURE 6. Photoacoustic measurements for metastatic and benign LNs. (A) Representative ultrasound, spectroscopic photoacoustic, fluorescence, and histology images of benign and metastatic LNs. Photoacoustic signals corresponding to pan800 and oxy- and deoxyhemoglobin have been spectrally unmixed. All scale bars are 5 mm. (B) Quantitative analysis of PAMI signal using pan800 avg. (C) Quantitative analysis of PAMI signal using pan800 avg thresh. US = ultrasound.

1.00–1.00). No difference of average total hemoglobin signal was found between metastatic and benign LNs (56,596 ± 31,158 a.u. vs. 43,026 ± 32,645 a.u., $P > 0.05$; Supplemental Fig. 2A). Similarly, no difference in average total oxygen saturation was found between metastatic and benign LNs (39.0% ± 22.8% vs. 39.2% ± 16.5%, $P > 0.05$; Supplemental Fig. 2B).

Heterogeneity of Photoacoustic Signal in Metastatic LNs

To assess the heterogeneity of the pan800 distribution in metastatic and benign LNs, further analysis was performed using the ratio of pan800 avg thresh to pan800 avg in the LNs. Figure 7A shows a representative metastatic LN in a patient with oral squamous cell carcinoma, in which the strong signal intensity was mainly detected in the nodal metastasis found on final pathologic examination. Examining the ratio of PAMI signals (pan800 avg thresh to pan800 avg) showed a significant difference between metastatic LNs and benign LNs, at 11.6 ± 13.4 versus 1.8 ± 0.7, respectively ($P < 0.01$; Fig. 7B). ROC evaluation showed that the AUC for the ratio of pan800 avg thresh to pan800 avg was 0.96 (95% CI, 0.91–1.00).

DISCUSSION

LN metastasis in an essential prognostic factor in HNSCC; however, early detection in normal-sized LNs (<10 mm diameter) remains challenging. Although PAMI has been shown to provide sufficient contrast and spatial resolution at significantly higher imaging depths than standard optical techniques, there have been limited clinical use and no reports of early detection of LN metastasis using PAMI with systemically circulated, molecularly specific agents in the clinical setting (*25,26*). To overcome the clinical challenge in early detection of small metastatic LNs (occult LNs), we assessed PAMI of resected LNs in HNSCC patients with a systemically administered IRDye800CW-labeled anti-EGFR antibody. After evaluation and validation of pan800 in a phantom setup, ex vivo PAMI and fluorescence assessment of human LNs was performed to identify occult metastatic disease in LNs.

The results of the current study demonstrate the feasibility of PAMI using a systemically administered tumor-specific antibody labeled with IRDye800CW for identification of LN metastasis in patients with HNSCC. To the best of our knowledge, this is the first report on the use of fluorescence imaging and PAMI after an intravenous injection of a tumor-specific antibody–dye conjugate to identify the LN metastases. Our results suggest that PAMI of IRDye800CW-labeled compounds has great potential to improve identification of LN metastasis and to change LN management during surgery.

PAMI allows for high-resolution imaging of optical absorption at depth (≤5 cm) (*27,28*), whereas fluorescence imaging provides high sensitivity to the contrast agent. Several fluorescent dyes, including indocyanine green, IRDye800CW, and methylene blue, are used for PAMI for noninvasive tumor detection passively via the enhanced permeability and retention effect (*29–31*). However, these dyes lack molecular specificity and are rapidly cleared from the circulation (*32*). Currently, several IRDye800CW-conjugated antibodies are under investigation for fluorescence-guided surgery to identify solid malignancies, with reasonable sensitivity and specificity reported for tumor identification in primary tumors and metastatic disease (*33–37*). Additionally, antibody–dye conjugates are thought to be optimal tumor-enhancement tracers in PAMI. This study indicated that PAMI of pan800 might be able to provide additional, complementary, information to conventional fluorescence imaging, such as enhanced imaging resolution at depth. Importantly, the safety of these IRDye800CW-labeled antibodies does not seem to differ from the safety of their native state (*20*), making them ideal to leverage in clinical applications of PAMI. To demonstrate the potential clinical value, we translated this technology from bench to bedside, performing PAMI on human neck specimens from HNSCC patients receiving anti-EGFR antibody conjugated with a NIR dye for improved identification of small metastatic LNs.

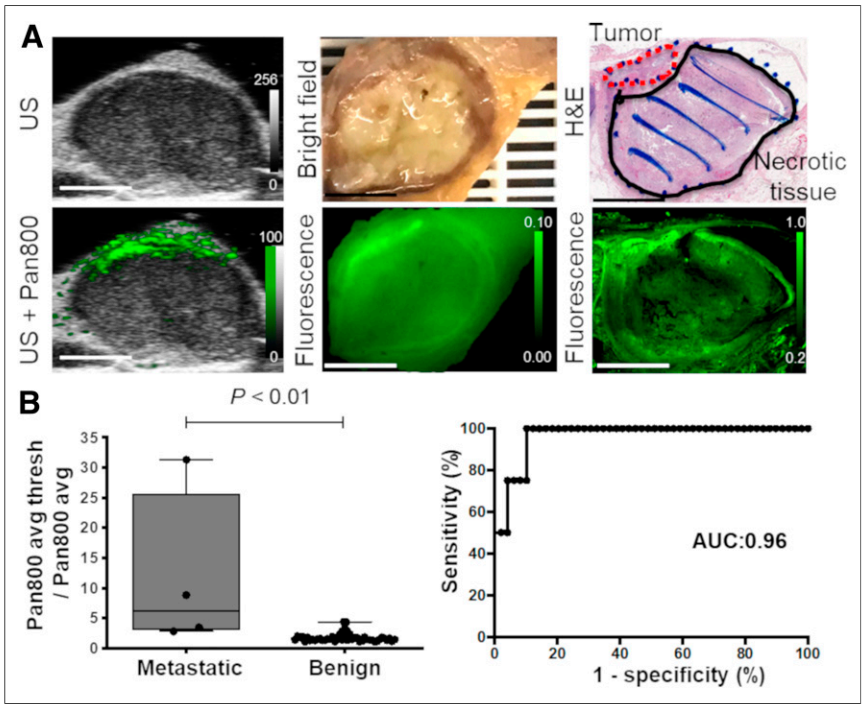

FIGURE 7. Heterogeneity of pan800 in metastatic LNs. (A) Representative ultrasound, photoacoustic, fluorescence, and histology images of metastatic LN. All scale bars are 5 mm. (B) Quantitative and ROC analysis of ratio of PAMI signal using pan800 avg thresh to pan800 avg to differentiate benign from metastatic LNs. US = ultrasound.

First, the feasibility and sensitivity of imaging pan800 with PAMI was tested in a tumor-mimicking phantom setup before a clinical application of PAMI. Not only was PAMI able to detect small concentrations of pan800 (1.2 nM), but it was also able to detect similarly small amounts in a scattering (optically and acoustically) and absorbing (optically) tissue-mimicking phantom. The constructed optical absorption spectrum of pan800 was found to have dual peaks at wavelengths sufficiently different from those of hemoglobin, indicating it can be spectroscopically resolved from within a background of hemoglobin-based signal (i.e., tissue). Using the photoacoustic multispectral unmixing mode in vivo would allow detection of the infused drug independently

from background blood signals, giving real-time molecular information from human tissue.

After in vitro verification, photoacoustic and fluorescence molecular imaging of surgically resected neck specimens containing several LNs was undertaken. Both imaging modalities can accurately differentiate between LNs containing occult metastases and benign LNs in an ex vivo scenario. In an in vivo, intraoperative, scenario, this differentiation ability could change. Fluorescence imaging suffers from low resolution and low penetration depth due to tissue optical scattering, leading to variations in signal dependent on imaging angle as demonstrated here in the preresection and whole-neck-specimen fluorescence images in Figure 4. Notably, the photoacoustic analyses performed here were from LNs before removal from the neck specimen and, therefore, with additional imaging depth and background tissue, whereas the fluorescence quantitative analysis was on individual LNs after removal from the neck specimen. Interestingly, the higher resolution of PAMI allowed for more nuanced quantitative assessment of the molecular imaging signal. Comparison of the ratio of pan800 signal within these regions (highest 10% of the signal) over the overall average pan800 signal allowed for highly accurate differentiation between normal and occult LNs (AUC, 0.96). Although examining the top 10% of pan800 signal also allowed for excellent differentiation in this well-controlled, ex vivo scenario, examining the heterogeneity ratio would allow for metastatic analysis regardless of intra- and interpatient variability in drug dosage, as well as without preinfusion conformational imaging. Taken together, photoacoustic and fluorescence molecular imaging may represent the ideal intraoperative multimodality technique, providing a high-sensitivity large field of view (fluorescence) with high-resolution images at depth (photoacoustic) when needed.

Additionally, high-resolution ultrasound was shown to be highly accurate in measuring the size of the LNs when compared with histologically determined size ($R^2 = 0.83$) and may identify suggestive nodes by size. With PAMI, it was possible to quantify the relative amounts of hemoglobin and the oxygen saturation within LNs, which previously were shown to be indicators of metastatic potential (*29*), although in the current study no differences were found between benign and metastatic LNs, as can be attributed to the ex vivo nature of the study or the low number of LN metastases. To further validate the clinical feasibility of PAMI, evaluation of LN characterization needs to be tested in a larger study population in an intraoperative, in vivo, setting. This effort would be aided greatly by further instrumentation development and application, such as handheld photoacoustic transducers that can image in 3 dimensions in real time, to accelerate clinical implementation of these imaging approaches.

CONCLUSION

This pilot study demonstrated the feasibility of a clinical application of PAMI using a tumor-specific IRDye800CW-labeled antibody to identify occult LN metastases in HNSCC patients. These results suggest that a heterogeneous distribution of the antibody–dye conjugate within LNs could be an essential indicator for identifying metastatic disease and that PAMI of IRDye800CW-labeled compounds has great potential to improve identification of LN metastases and to change surgical LN management. Real-time PAMI in an in vivo setting is required to confirm these initial findings.

DISCLOSURE

Eben L. Rosenthal acts as a consultant for LI-COR Biosciences Inc. and has equipment loans from this company. The Vevo Lazr-X equipment was provided for this study by Fujifilm VisualSonics. This work was supported in part by the Stanford Comprehensive Cancer Center, the Stanford University School of Medicine Medical Scholars Program, the Netherlands Organization for Scientific Research (Rubicon; 019.171LW.022), the National Institutes of Health (National Cancer Institute [R01CA190306] and National Institute for Biomedical Imaging and Bioengineering [R21EB022214 and K99EB023279]), and a scientific research grant from the Yokoyama Foundation for Clinical Pharmacology (YRY-1702). No other potential conflict of interest relevant to this article was reported.

KEY POINTS

QUESTION: Can spectroscopic PAMI combined with a systemically administered tumor-specific antibody–IRDye800CW conjugate identify occult LN metastasis in patients with HNSCC?

PERTINENT FINDINGS: After in vitro verification, photoacoustic and fluorescence molecular imaging of surgically resected neck specimens containing several LNs was undertaken. PAMI with a systemically administered IRDye800CW-labeled anti-EGFR antibody could accurately differentiate between LNs containing occult metastases and benign LNs in an ex vivo scenario.

IMPLICATIONS FOR PATIENT CARE: PAMI of IRDye800CW-labeled compounds has great potential to improve identification of LN metastases and to change LN management during surgery.

REFERENCES

1. Argiris A, Karamouzis MV, Raben D, Ferris RL. Head and neck cancer. *Lancet.* 2008;371:1695–1709.
2. Sun J, Li B, Li CJ, et al. Computed tomography versus magnetic resonance imaging for diagnosing cervical lymph node metastasis of head and neck cancer: a systematic review and meta-analysis. *Onco Targets Ther.* 2015;8:1291–1313.
3. van den Brekel MWM. Lymph node metastases: CT and MRI. *Eur J Radiol.* 2000;33:230–238.
4. Chong V. Cervical lymphadenopathy: what radiologists need to know. *Cancer Imaging.* 2004;4:116–120.
5. Forghani R, Yu E, Levental M, Som PM, Curtin HD. Imaging evaluation of lymphadenopathy and patterns of lymph node spread in head and neck cancer. *Expert Rev Anticancer Ther.* 2015;15:207–224.
6. Divi V, Chen MM, Nussenbaum B, et al. Lymph node count from neck dissection predicts mortality in head and neck cancer. *J Clin Oncol.* 2016;34:3892–3897.
7. D'Cruz AK, Vaish R, Kapre N, et al. Elective versus therapeutic neck dissection in node-negative oral cancer. *N Engl J Med.* 2015;373:521–529.
8. Alkureishi LWT, Burak Z, Alvarez JA, et al. Joint practice guidelines for radionuclide lymphoscintigraphy for sentinel node localization in oral/oropharyngeal squamous cell carcinoma. *Eur J Nucl Med Mol Imaging.* 2009;36:1915–1936.
9. Seethala RR. Current state of neck dissection in the United States. *Head Neck Pathol.* 2009;3:238–245.
10. Carlson RO, Amirahmadi F, Hernandez JS. A primer on the cost of quality for improvement of laboratory and pathology specimen processes. *Am J Clin Pathol.* 2012;138:347–354.
11. Nishio N, van den Berg NS, van Keulen S, et al. Optical molecular imaging can differentiate metastatic from benign lymph nodes in head and neck cancer. *Nat Commun.* 2019;10:5044.
12. van Keulen S, van den Berg NS, Nishio N, et al. Rapid, non-invasive fluorescence margin assessment: Optical specimen mapping in oral squamous cell carcinoma. *Oral Oncol.* 2019;88:58–65.
13. Bell AG. On the production and reproduction of sound by light. *Am J Sci.* 1880;20:305–324.

14. Beard P. Biomedical photoacoustic imaging. *Interface Focus.* 2011;1:602–631.
15. Kim S, Chen Y-S, Luke GP, Emelianov SY. In vivo three-dimensional spectroscopic photoacoustic imaging for monitoring nanoparticle delivery. *Biomed Opt Express.* 2011;2:2540–2550.
16. Wang LV, Wu H. Biomedical Optics: Principles and Imaging. John Wiley and Sons, Inc.; 2007:283–309.
17. Wilson KE, Bachawal SV, Abou-Elkacem L, et al. Spectroscopic photoacoustic molecular imaging of breast cancer using a B7-H3-targeted ICG contrast agent. *Theranostics.* 2017;7:1463–1476.
18. Wilson KE, Bachawal S, Willmann JK. Intraoperative resection guidance with photoacoustic and fluorescence molecular imaging using an anti-B7-H3 antibody-indocyanine green dual contrast agent. *Clin Cancer Res.* 2018;24:3572–3582.
19. Bachawal S, Bean GR, Krings G, Wilson KE. Evaluation of ductal carcinoma in situ grade via triple-modal molecular imaging of B7-H3 expression. *NPJ Breast Cancer.* 2020;6:14.
20. Gao RW, Teraphongphom N, de Boer E, et al. Safety of panitumumab-IRDye800CW and cetuximab-IRDye800CW for fluorescence-guided surgical navigation in head and neck cancers. *Theranostics.* 2018;8:2488–2495.
21. Cook JR, Bouchard RR, Emelianov SY. Tissue-mimicking phantoms for photoacoustic and ultrasonic imaging. *Biomed Opt Express.* 2011;2:3193–3206.
22. Hildebrandt U, Klein T, Feifel G, Schwarz HP, Koch B, Schmitt RM. Endosonography of pararectal lymph nodes. *Dis Colon Rectum.* 1990;33:863–868.
23. Nishio N, van Keulen S, van den Berg NS, et al. Probe-based fluorescence dosimetry of an antibody-dye conjugate to identify head and neck cancer as a first step to fluorescence-guided tissue preselection for pathological assessment. *Head Neck.* 2020;42:59–66.
24. van Keulen S, Nishio N, Fakurnejad S, et al. Intraoperative tumor assessment using real-time molecular imaging in head and neck cancer patients. *J Am Coll Surg.* 2019;229:560–567.
25. Fu Q, Zhu R, Song J, Yang H, Chen X. Photoacoustic imaging: contrast agents and their biomedical applications. *Adv Mater.* 2019;31:e1805875.
26. Steinberg I, Huland DM, Vermesh O, Frostig HE, Tummers WS, Gambhir SS. Photoacoustic clinical imaging. *Photoacoustics.* 2019;14:77–98.
27. Beard P. Biomedical photoacoustic imaging. *Interface Focus.* 2011;1:602–631.
28. Wang LV, Hu S. Photoacoustic tomography: in vivo imaging from organelles to organs. *Science.* 2012;335:1458–1462.
29. Gargiulo S, Albanese S, Mancini M. State-of-the-art preclinical photoacoustic imaging in oncology: recent advances in cancer theranostics. *Contrast Media Mol Imaging.* 2019;2019:5080267.
30. Kim C, Favazza C, Wang LV. In vivo photoacoustic tomography of chemicals: high-resolution functional and molecular optical imaging at new depths. *Chem Rev.* 2010;110:2756–2782.
31. Kothapalli SR, Sonn GA, Choe JW, et al. Simultaneous transrectal ultrasound and photoacoustic human prostate imaging. *Sci Transl Med.* 2019;11:507.
32. Capozza M, Blasi F, Valbusa G, et al. Photoacoustic imaging of integrin-over-expressing tumors using a novel ICG-based contrast agent in mice. *Photoacoustics.* 2018;11:36–45.
33. Gao RW, Teraphongphom NT, van den Berg NS, et al. Determination of tumor margins with surgical specimen mapping using near-infrared fluorescence. *Cancer Res.* 2018;78:5144–5154.
34. Lamberts LE, Koch M, de Jong JS, et al. Tumor-specific uptake of fluorescent bevacizumab–IRDye800CW microdosing in patients with primary breast cancer: a phase I feasibility study. *Clin Cancer Res.* 2017;23:2730–2741.
35. van Keulen S, Nishio N, Fakurnejad S, et al. The clinical application of fluorescence-guided surgery in head and neck cancer. *J Nucl Med.* 2019;60:758–763.
36. van Keulen S, Nishio N, Birkeland A, et al. The sentinel margin: intraoperative ex vivo specimen mapping using relative fluorescence intensity. *Clin Cancer Res.* 2019;25:4656–4662.
37. Koller M, Qiu S-Q, Linssen MD, et al. Implementation and benchmarking of a novel analytical framework to clinically evaluate tumor-specific fluorescent tracers. *Nat Commun.* 2018;9:3739.